JASA ARTICLE

Modal formulation and paraxial approximation for acoustic wave propagation in waveguides with surface perturbations

Josselin Garnier[1,a)] and Philippe Roux[2]
[1]Centre de Mathématiques Appliquées, Ecole Polytechnique, Institut Polytechnique de Paris, Palaiseau, France
[2]ISTerre, Université Grenoble Alpes, Université Savoie Mont Blanc, Centre National de la Recherche Scientifique, Institut de Recherche pour le Développement, Université Gustave Eiffel, Grenoble INP, Grenoble, France

ABSTRACT:
We propose a modal approach developed in the framework of the paraxial approximation to investigate the effects of deterministic surface perturbations in a planar waveguide. In the first part, the sensitivity of the modal amplitudes is theoretically formulated for a three-dimensional perturbation at the air–water interface. When applied to a broadband ultrasonic signal in a laboratory tank experiment, this approach results in travel-time and amplitude fluctuations that are successfully compared to experimental data recorded between two vertical source–receiver arrays that span the ultrasonic waveguide. The nonlinear shape of the modal amplitude fluctuations is of particular interest and is due to the three-dimensional nature of the surface perturbation. In the second part, a time-harmonic inversion method is built in the paraxial single-scattering approximation to image the dynamic surface perturbation from the modal transmission matrix between two source–receiver arrays. Again, the inversion results for capillary-gravity surface perturbations are successfully compared to similar inversions performed from experimental data processed with a complete set of eigenbeams extracted between the two arrays.
https://doi.org/10.1121/10.0010533

(Received 15 January 2022; revised 23 April 2022; accepted 27 April 2022; published online 16 May 2022)
[Editor: Agnes Maurel] Pages: 3239–3254

I. INTRODUCTION

Surface scattering in a waveguide involves the combination of waveguide propagation and scattering physics, both of which have been extensively studied separately. The rough and time-varying nature of the sea surface scatters sound in complex ways. For instance, the crest of a surface wave can act like a concave acoustic lens to focus sound so that the surface-reflected multi-path arrival has an intensity greater than that of the direct arrival. Arrival times vary as the gross elevation of the smaller waves responsible for acoustic focusing is modulated by large-scale wave features, such as swell.

From theory and simulation, a series of studies in the late 1980s provided useful descriptors of sea-surface scattering using Kirchhoff and perturbation approximations.[1,2] The new trend in surface scattering is to predict and invert for a deterministic gravity wave, taking advantage of the sensitivity of the amplitude and phase modulations of the incident acoustic wave to the local elevation and curvature of the surface near the specular reflection points.[3–7] These studies were motivated by the impact of surface scattering on underwater acoustics applications, such as communication systems or sonar in shallow waters.[8,9]

The dynamic imaging of a deterministic gravity wave propagating at an air–water interface requires continuous sampling of every point at this interface. This sampling can be done acoustically using waves that propagate in the water column but have specular reflection points that fully scan the air–water interface. The use of many source–receiver pairs multiplies the number of specular reflection points, which allows for better sampling of the air–water interface. Moreover, the multi-path propagation in the waveguide also contributes to improved surface sampling, as each eigenray that bounces several times at the surface naturally increases its sensitivity to any surface deformation.[10] Following this methodology, there were recent experimental demonstrations of dynamic imaging of a deterministic capillary-gravity wave in an ultrasonic waveguide from ultrasonic source and receiver arrays that face each other in a 1-m-long, 5-cm-deep fluid waveguide and have frequencies in the MHz range. Through a double-beamforming (DBF) process,[11,12] a large set of acoustic multi-reverberated beams that interact with the air–water interface were isolated and identified. The travel-times, amplitudes, and source–receiver angles of a few thousand eigenbeams are natural observables for eigenbeams that are measured when the capillary-gravity wave travels through the source–receiver plane. Linear inversion of these observables leads to accurate spatial–temporal patterns of the surface deformation[13,14] with the spatial resolution bounded by both the acoustic wavelength and the extent of the source-to-receiver Fresnel zone of the acoustic wave at the surface.

The present study aims at revisiting the above-mentioned eigenbeam methodology using a newly developed modal approach for the dynamic imaging of a deterministic

[a)]Electronic mail: josselin.garnier@polytechnique.edu

JASA

gravity wave in a waveguide. Using the eigenmodes of the waveguide to invert for a surface perturbation might appear counterintuitive because the modes are classically defined as an invariant of the waveguide along the waveguide axis propagation. However, the eigenmodes are also a basis for the acoustic wavefield: as such, the modal transmission matrix between the source array and the receiver array contains all of the elements that allow reconstruction of the profile of the waveguide surface.

The objective of this paper is twofold. In the first part, the modal approach is rapidly revisited in a plane waveguide. The sensitivity of the modal amplitudes is theoretically formulated for a three-dimensional perturbation at the air–water interface in the paraxial approximation. The paraxial approximation holds when the typical wavelength is much smaller than the typical scale of variations of the surface perturbations, which is itself much smaller than the propagation distance. When applied to a broadband ultrasonic signal, this approach results in travel-time and amplitude fluctuations that are compared successfully to experimental data.[4] In the second part, a time-harmonic method is built in the paraxial single-scattering approximation to image the dynamic surface perturbations from the modal amplitudes of the signals collected at a high frame rate between the source and receiver arrays. Again, inversion results for two-dimensional and three-dimensional surface perturbations are successfully compared to similar inversions performed from the eigenbeam methodology[4,13] with the same experimental data.

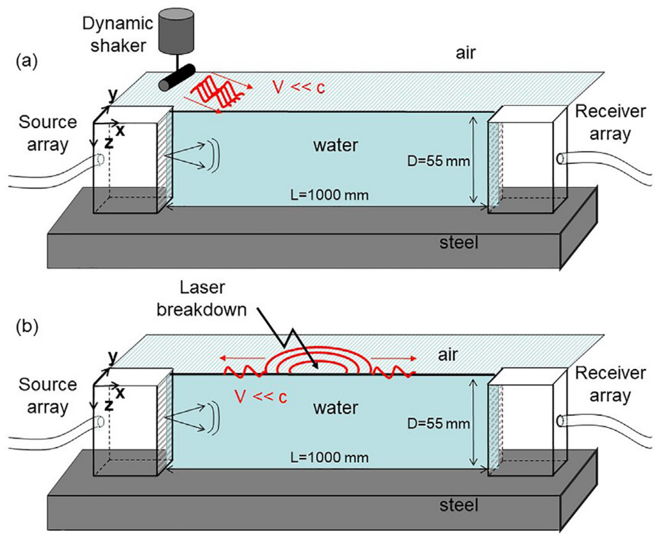

FIG. 1. (Color online) Schematic of the experimental setup designed to image a traveling gravity-capillary wave on the surface of the waveguide. Vertical 64-element source and receiver arrays face each other in a 1-m-long, 55-mm-deep water waveguide. The waveguide dimensions are large compared to the 1.5 mm wavelength of the ultrasonic wave. The bottom is made of steel, which allows for perfect reflection at this interface. The transfer matrix of the waveguide (between the elements of the source and receiver arrays) is recorded at a rate of 100 frames/s over 5 s. (a) Modified from Ref. 4. A computer-controlled dynamic shaker is attached to a Plexiglas cylinder placed at the air–water interface on the side of the waveguide. This device generates impulsive gravity waves that cross the source–receiver axis in a few seconds. (b) Modified from Ref. 13. The surface waves are caused by laser-induced breakdown (lightning-shaped arrow) in the center of the waveguide, which generates contra-propagative waves along the axis of the waveguide.

II. WAVE PROPAGATION IN AN ACOUSTIC WAVEGUIDE

We consider acoustic wave propagation in a planar waveguide, as illustrated in Fig. 1. We denote by $x \in \mathbb{R}$ the range as the main axis of the waveguide. The medium is unbounded in the cross-range direction y, but it is confined in depth z by two planar and parallel boundaries that trap the waves, thus creating the waveguide effect. The acoustic pressure field denoted by $p(t,x,y,z)$ satisfies the wave equation

$$\left[\partial_x^2+\partial_y^2+\partial_z^2-\frac{1}{c_o^2}\partial_t^2\right]p(t,x,y,z)=f(t,z)\delta(x)\delta(y) \tag{1}$$

inside the waveguide, which is filled with a medium with homogeneous wave speed c_o. The pulsed excitation is due to a vertical linear source array localized in the line $x=0, y=0$, and the wavefield is received at distance L on a vertical linear receiver array localized in the line $x=L, y=0$. The bottom at $z=0$ is perfectly flat and rigid: $\partial_z p(t,x,y,z=0)=0$. The pressure release boundary condition at the perturbed top boundary $p(t,x,y,z=T(x,y))=0$ means that the top boundary $z=T(x,y)$ has small fluctuations around the mean depth $\mathcal{D}$, $|T(x,y)-\mathcal{D}| \ll \mathcal{D}$, localized in the region $x \in (0,L)$. The boundary fluctuations are modeled with the smooth and bounded function μ,

$$T(x,y)=\mathcal{D}[1+\mu(x,y)]. \tag{2}$$

The goals of our study are (1) to quantify the effects of acoustic scattering by the surface perturbation μ, (2) to experimentally compare the modal-based perturbation approach to ultrasonic data recorded by the receiver array, and (3) to design imaging functions that estimate the surface perturbation from the ultrasonic signals recorded between the source–receiver arrays. In the analysis, the surface perturbation μ is assumed to be time-independent with respect to the ultrasonic wave sampling. This assumption is valid in our experimental configurations, as the velocity of the gravity waves (<1 m/s) is much smaller than the velocity of the acoustic waves ($\simeq$ 1500 m/s), so the surface perturbation can be considered as frozen during the acquisition of the transfer matrix from all of the elements of the source array to all of the elements of the receiver array.

III. PARAXIAL APPROXIMATION IN A PERFECT WAVEGUIDE

We consider the paraxial regime $L \gg \mathcal{D} \gg \lambda_o$, where $\lambda_o = 2\pi/k$ is the central wavelength. In this section, we consider the case $\mu \equiv 0$. Assuming $x \gg \lambda_o$ and $|y| \lesssim \sqrt{\lambda_o x}$, the pressure field in the paraxial approximation has the form

$$\hat{p}_o(\omega,x,y,z) \approx \sum_{j=1}^{N(\omega)} \phi_j(\omega,z)\hat{a}_{j,o}(\omega,x,y)e^{i\beta_j(\omega)x}, \tag{3}$$

with explicit expressions of the eigenfunctions ϕ_j, which are independent of the frequency in a perfect waveguide,

$$\phi_j(z) = \sqrt{\frac{2}{\mathcal{D}}}\cos\left[\pi\left(j-\frac{1}{2}\right)\frac{z}{\mathcal{D}}\right] \tag{4}$$

and

$$\hat{a}_{j,o}(\omega,x,y) = \frac{e^{-3i\pi/4}}{2\sqrt{2\pi\beta_j(\omega)x}}\exp\left[\frac{i\beta_j(\omega)y^2}{2x}\right]\hat{f}_j(\omega), \tag{5}$$

for $j = 1,\ldots,N$ that correspond to the $N = [k\mathcal{D}/\pi]$ propagative modes in the waveguide, with $k = \omega/c_o$. In Eqs. (3) and (5), we introduce the modal wavenumber $\beta_j(\omega) = \sqrt{|\lambda_j(\omega)|}$ with eigenvalues defined as

$$\lambda_j(\omega) = \left(\frac{\pi}{\mathcal{D}}\right)^2\left[\left(\frac{k\mathcal{D}}{\pi}\right)^2 - \left(j-\frac{1}{2}\right)^2\right] \tag{6}$$

and the coefficients of the source profile in the basis of the eigenfunctions,

$$\hat{f}_j(\omega) = \int_0^{\mathcal{D}} dz\,\phi_j(z)\hat{f}(\omega,z). \tag{7}$$

The Fourier transform of the source,

$$\hat{f}(\omega,z) = \int_{-\infty}^{\infty} dt f(t,z)e^{i\omega t}, \tag{8}$$

is assumed to be compactly supported (for positive frequencies) in $[\omega_o - B/2, \omega_o + B/2]$. Here, ω_o is the central frequency, and B is the bandwidth.

In short, the pressure field in Eq. (3) is a superposition of forward going modes that are propagating in the range direction x, with slowly varying amplitudes $\hat{a}_{j,o}$ given by Eq. (5). For $j = 1,\ldots,N$, these modal amplitudes solve the paraxial equations,

$$\left[2i\beta_j(\omega)\partial_x + \partial_y^2\right]\hat{a}_{j,o}(\omega,x,y) = 0, \tag{9}$$

with initial conditions

$$\hat{a}_{j,o}(\omega,x=0,y) = \frac{\hat{f}_j(\omega)}{2i\beta_j(\omega)}\delta(y). \tag{10}$$

In the case of broadband source excitation, the wave signals recorded by a receiver located at depth z_r for a source of the form

$$f(t,z) = F(z)f_o(Bt)e^{-i\omega_0 t} + c.c., \tag{11}$$

with $B \ll \omega_o$, is

$$p_o(t,L,0,z_r) = \frac{1}{2\pi}\int\sum_{j=1}^{N(\omega)}\phi_j(z_r)\hat{a}_{j,o}(\omega,L,0) \times e^{i\beta_j(\omega)L - i\omega t}d\omega + c.c., \tag{12}$$

$$\hat{a}_{j,o}(\omega,L,0) = \frac{e^{-3i\pi/4}F_j}{2\sqrt{2\pi\beta_j(\omega)L}}\frac{1}{B}\hat{f}_o\left(\frac{\omega-\omega_o}{B}\right), \tag{13}$$

with $F_j = \int_0^{\mathcal{D}} F(z)\phi_j(z)dz$. Therefore, the signal has the form of a train of short pulses,

$$p_o(t,L,0,z_r) = \sum_{j=1}^{N(\omega_o)} A_{j,o}\phi_j(z_r)f_o\big(B(t-T_{j,o})\big) + c.c., \tag{14}$$

which arrive at the travel-time of the jth mode,

$$T_{j,o} = \beta_j'(\omega_o)L \overset{j \ll N(\omega_o)}{\simeq} \frac{L}{c_o} + \frac{L}{c_o}\frac{\pi^2\left(j-\frac{1}{2}\right)^2}{2k_o^2\mathcal{D}^2}, \tag{15}$$

with $k_o = \omega_o/c_o$, and with amplitude

$$A_{j,o} = \frac{e^{i\beta_j(\omega_o)L - i\omega_o t - 3i\pi/4}}{2\sqrt{2\pi\beta_j(\omega_o)L}}F_j. \tag{16}$$

IV. PARAXIAL APPROXIMATION IN A ROUGH WAVEGUIDE

In the paraxial regime and in the presence of a surface perturbation [Eq. (2)], the pressure field takes the form (see details in Appendix A)

$$\hat{p}(\omega,x,y,z) = \sum_{j=1}^{N(\omega)}\phi_j(z)\hat{a}_j(\omega,x,y)e^{i\beta_j(\omega)x}. \tag{17}$$

The modal amplitudes satisfy the leading order of the Schrödinger-type equations,

$$\partial_x\hat{a}_j(\omega,x,y) = \frac{i}{2\beta_j(\omega)}\partial_y^2\hat{a}_j - \frac{i\,q_{jj}}{2\beta_j(\omega)}\mu(x,y)\hat{a}_j, \tag{18}$$

for $x > 0$, and the initial conditions

$$\hat{a}_j(\omega,x=0,y) = \frac{\hat{f}_j(\omega)}{2i\beta_j(\omega)}\delta(y), \quad j = 1,\ldots,N. \tag{19}$$

The coefficients q_{jj} are defined by

$$q_{jj} = 2\int_0^{\mathcal{D}} dz\,\phi_j(z)\phi_j''(z) = -2\left(\frac{\pi}{\mathcal{D}}\right)^2\left(j-\frac{1}{2}\right)^2. \tag{20}$$

To analyze beam propagation in rough waveguides and to obtain Eq. (18), we introduce in Appendix A 1 a change of coordinates that flattens the perturbed surface boundary. The mapped wave field then satisfies a wave equation perturbed by a differential operator with rough coefficients. We show in Appendix A 2 that the solution can be written as a superposition of the ideal (unperturbed) waveguide modes with range-dependent modal amplitudes that solve the paraxial Eq. (18) driven by the function μ. These modal amplitudes model the cumulative scattering effects of the perturbed surface. In Eq. (18), we keep only the leading-order terms that describe the evolutions of the modal amplitudes and that explain the forms of the travel-time and amplitude perturbations observed in the experiments [see Eqs. (26) and (27) below]. We neglect higher-order terms that describe mode conversion and that will be important for the resolution of the inverse problem in Sec. VI.

The wave field recorded at distance L on the receiver array is sensitive to the perturbation μ only in a tube with radius in y on the order of $\sqrt{\lambda_o L}$ (the Fresnel zone). We assume that the transverse scale of the perturbation μ is on the order of or larger than $\sqrt{\lambda_o L}$. We can therefore expand

$$\mu(x,y) = \mu_0(x) + \frac{y}{\sqrt{\lambda_o L}}\mu_1(x) + \frac{y^2}{\lambda_o L}\mu_2(x), \tag{21}$$

where μ_j are compactly supported in $[L_0, L_1] \subset (0, L)$. Under such circumstances, Appendix B 1 shows that the approximate expression of the modal amplitudes at $x = L$, $y = 0$ is given by

$$\hat{a}_j(\omega, L, 0) = \frac{\hat{A}_{j,o}(\omega, L)}{\sqrt{1 - \frac{q_{jj}}{\beta_j(\omega)^2}\frac{\nu_2}{\lambda_o}\frac{L_1(L-L_1)}{L^2}}} \times \exp\left(-i\frac{q_{jj}}{2\beta_j(\omega)}\nu_0\right), \tag{22}$$

where

$$\hat{A}_{j,o}(\omega, L) = \frac{e^{-3i\pi/4}}{2\sqrt{2\pi\beta_j(\omega)L}}\hat{f}_j(\omega), \quad \nu_l = \int_{L_0}^{L_1}\mu_l(x)dx. \tag{23}$$

The wave signals recorded by a receiver located at depth z_r when there is a source of the form (11) are

$$p(t, L, 0, z_r) = \frac{1}{2\pi}\int\sum_{j=1}^{N(\omega)}\phi_j(z_r)\hat{a}_j(\omega, L, 0) \times e^{i\beta_j(\omega)L - i\omega t}d\omega + c.c., \tag{24}$$

where $\hat{a}_j(\omega, L, 0)$ is given by Eqs. (22) and (23) with $\hat{f}_j(\omega) = (F_j/B)\hat{f}_o((\omega - \omega_o)/B)$. Therefore, the signal has the form of a train of short pulses,

$$p(t, L, 0, z_r) = \sum_{j=1}^{N(\omega_o)} A_j\phi_j(z_r)f_o\big(B(t - T_j)\big) + c.c., \tag{25}$$

that arrive at the perturbed travel-times of the modes,

$$\begin{aligned} T_j &= \beta_j'(\omega_o)L + \frac{q_{jj}}{2\beta_j(\omega_o)^2}\beta_j'(\omega_o)\nu_0 \\ &= T_{j,o}\left(1 + \frac{q_{jj}}{2\beta_j(\omega_o)^2}\frac{\nu_0}{L}\right) \\ &\overset{j\ll N(\omega_o)}{\simeq} T_{j,o}\left(1 - \left(j - \frac{1}{2}\right)^2\frac{\pi^2\nu_0}{k_o^2\mathcal{D}^2 L}\right), \end{aligned} \tag{26}$$

where $T_{j,o}$ is the unperturbed arrival time of the jth mode [Eq. (15)] and with the perturbed amplitude

$$\begin{aligned} A_j &= \frac{A_{j,o}}{\sqrt{1 - \frac{q_{jj}}{\beta_j(\omega)^2}\frac{\nu_2}{\lambda_o}\frac{L_1(L-L_1)}{L^2}}} \\ &\overset{j\ll N(\omega_o)}{\simeq} \frac{A_{j,o}}{\sqrt{1 + \left(j - \frac{1}{2}\right)^2\frac{\pi\nu_2 L_1(L-L_1)}{k_o\mathcal{D}^2 L^2}}}, \end{aligned} \tag{27}$$

where $A_{j,o}$ is the unperturbed amplitude of the jth mode [Eq. (16)]. Note that the travel-time perturbation is linear in ν_0, while the amplitude perturbation is not linear in ν_2. As a consequence, when the perturbation of the surface slowly evolves in time, as a periodic and harmonic function like a cosine, for instance, then the terms ν_j behave like a cosine and the travel-time perturbation behaves like a cosine, but the amplitude perturbation behaves like a nonharmonic function. This apparent nonlinear behavior of the amplitude perturbation results from linear propagation effects: the transverse curvature of the surface perturbation ν_2 can induce a quadratic wave front that acts as a lens and involves the focusing of the acoustic wave. This behavior is illustrated in Sec. V, devoted to the experimental data.

V. EXPERIMENTAL CONFIGURATION AND DATA ANALYSIS

The experimental setup is a variation of an ultrasonic Pekeris waveguide.[15] Two source–receiver ultrasonic arrays face each other in a small-scale shallow-water waveguide (Fig. 1). The waveguide depth is $\mathcal{D} = 55$ mm, and its length is $L = 1$ m. The bottom of the waveguide is steel and provides good reflection of ultrasonic waves. The arrays are composed of 64 transducers centered at 1 MHz with a 75% bandwidth. The ultrasonic signal transmitted by each piezo-transducer source is a broadband pulse of 1 μs at the central frequency of the transducer. The received signals spread over 80 μs after the direct arrival at $\simeq 680$ μs, which corresponds to $(L/\mathcal{D})\sqrt{(760/680)^2 - 1} \simeq 10$ reverberations on the waveguide boundaries.[4] On both arrays, the transducer dimensions are 0.75 mm along the vertical axis (that corresponds to half of the central wavelength) and 12 mm along the transverse axis. This feature naturally creates a collimated beam in the waveguide axis direction, which avoids side echoes from the tank walls. Recent studies[13,14] estimate the transverse size of the source-to-receiver Fresnel zone at ± 2 cm on each side of the waveguide axis.

https://doi.org/10.1121/10.0010533

Based on this experimental setup for ultrasonic waveguide propagation, the present study revisits this in the framework of the paraxial approximation for two experimental datasets that deal with surface perturbations at an air–water interface.

The first experiment (EXP1) is detailed in Ref. 4. A computer-controlled dynamic shaker is connected to a 20-cm-long, 2-cm-diameter Plexiglas cylinder that is half-immersed on the side of the acoustic waveguide, as shown in Fig. 1(a). The signal sent to the shaker is a Gaussian pulse that is centered at 3.5 Hz, with a $\simeq 40\%$ bandwidth, and generates impulsive capillary-gravity waves at the air–water interface. The cylinder axis is horizontal and tilted at $\simeq 40^\circ$ with respect to the source-to-receiver array axis. The capillary-gravity wave crosses the acoustic waveguide as a three-dimensional surface perturbation in a few seconds. The maximum wave height is controlled by the amplitude of the signal sent to the shaker and is on the order of a few millimeters. As the capillary-gravity wavelength λ_g (of a few centimeters) is much greater than the acoustic wavelength ($\lambda_o = 1.5$ mm), the surface-reflected acoustic waves should be sensitive to details in the surface deformation at spatial scales much smaller than λ_g.

The second experiment (EXP2) is detailed in Ref. 14. The surface of the waveguide is perturbed by a blast wave generated by laser-induced breakdown above the surface in the plane $y = 0$ and at the position $x \approx 0.56$ m [Fig. 1(b)]. The perturbation is localized and controllable by the power of the laser excitation and results in a circular surface wave. Due to the dimensions of the waveguide, this circular wave is seen by the ultrasonic source–receiver arrays as two counter-propagative capillary-gravity wave packets that expand from the center of the waveguide as a two-dimensional surface perturbation.

In both experiments, while the surface perturbation is traveling across the surface, the ultrasonic system records the transfer matrix of the waveguide between the source–receiver arrays at 100 times/s, over 5 s. By transfer matrix, we mean the complete set of 64×64 time-domain signals emitted by every source and received by every receiver of the two arrays.

The calculation of the perturbed and unperturbed travel-times $\{T_j, T_{j,0}\}$ and amplitudes $\{A_j, A_{j,0}\}$ defined for each mode in Eqs. (26) and (27) requires projection of the pressure wavefield onto the modal basis. In theory, the mode profiles $\phi_j(z)$ should be the theoretical eigenfunctions [Eq. (4)] in a perfect waveguide. In practice, the waveguide used in EXP1 and EXP2 can be approximated by a Pekeris waveguide. The actual mode profiles $\tilde{\phi}_j(z)$ are extracted for each mode from the waveguide transfer matrix $\hat{p}_o(\omega, x, y, z)$ recorded between the source and receiver arrays in the absence of surface perturbation. More precisely, the mode profiles $\tilde{\phi}_j(z)$ are obtained by optimizing the mode parameters numerically computed from a Pekeris waveguide model so as to maximize the output intensity of the experimental waveguide transfer matrix projected on the modes for both the source and receiver dimensions [Eq. (28)]. The optimization is carried out with respect to physical parameters, such as the waveguide depth $\mathcal{D}$ and steel bottom elastic properties for the Pekeris model, but also against geometrical parameters, such as the relative positions in depth of the 64-element source–receiver arrays in the water column.

Figure 2 shows the optimal projection of the transfer matrix on the mode profiles for the unperturbed waveguide with the plot of the mode profiles $\tilde{\phi}_j(z)$ for modes $j = 1$ to $j = 4$ on the source–receiver arrays. The travel-times $T_{j,0}$ and amplitudes $A_{j,0}$ are obtained directly from the maximum of the envelope of the transfer matrix projection for every mode, as calculated from the following equation:

$$\begin{aligned} A_{j,o} f_o\big(B(t - T_{j,o})\big) &= \int d\omega \int_0^{\mathcal{D}} dz_r \int_0^{\mathcal{D}} dz_s\, \tilde{\phi}_j(z_r)\tilde{\phi}_j(z_s) \\ &\quad \times \hat{p}_o(\omega, z_s, z_r, x = L, y = 0) e^{-i\omega t} + c.c., \end{aligned} \tag{28}$$

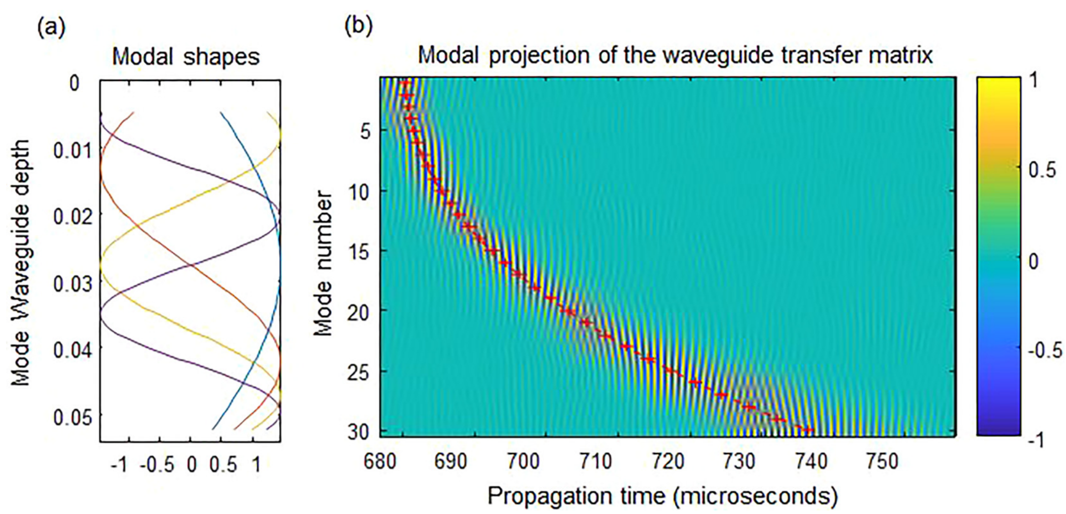

FIG. 2. (Color online) (a) Mode profiles $\tilde{\phi}_j(z)$ for modes 1–4 extracted from the transfer matrix data of the unperturbed waveguide. (b) Normalized projection of the unperturbed transfer matrix onto the mode profiles on both the source and receiver arrays. Note the delayed arrival times of the different modes (from mode 1 to mode 30) that correspond to the dispersion of the pressure field in the reverberated waveguide, as calculated from the source–receiver distance L and the modal group velocities (red square).

where $\hat{p}_o(\omega, x = L, y = 0, z_s, z_r)$ is the unperturbed pressure field between a source in z_s and a receiver in z_r, respectively. Using the actual mode profiles $\tilde{\phi}_j(z)$, the projections of the successive recorded transfer matrices lead to the extraction of the travel-times T_j [Eq. (26)] and amplitudes A_j [Eq. (27)], while the surface perturbation travels at the air–water interface.

In the experimental configuration of EXP1,[4] the dynamic shaker excites the half-immersed horizontal cylinder with three different voltages (amp1 = 1 V, amp2 = 2 V, amp3 = 3 V), thus creating increasing surface perturbations in each case. Due to the large bandwidth of the piezo-transducers, the transfer matrices can be studied at three different frequencies $\omega_o = 2\pi \times 0.5, 1, 1.5$ MHz and for each amplitude modulation of the surface perturbation.

In Fig. 3, we plot for mode 15 and at $\omega_o = 2\pi \times 1$ MHz the relative amplitude perturbation $A_j(t)/A_{j_0} - 1$ and the time perturbation $T_j(t) - T_{j0}$ as functions of the acquisition time t. Here, we assume that the surface perturbations vary as $p_1 \cos(p_2 t) \exp(-p_3 t^2)$ with respect to the slow time t (up to a time shift), and we adapt p_1, p_2, and p_3 to fit the observations. We find $p_1(amp1) \simeq p_1(amp2)/2 \simeq p_1(amp3)/3$, in

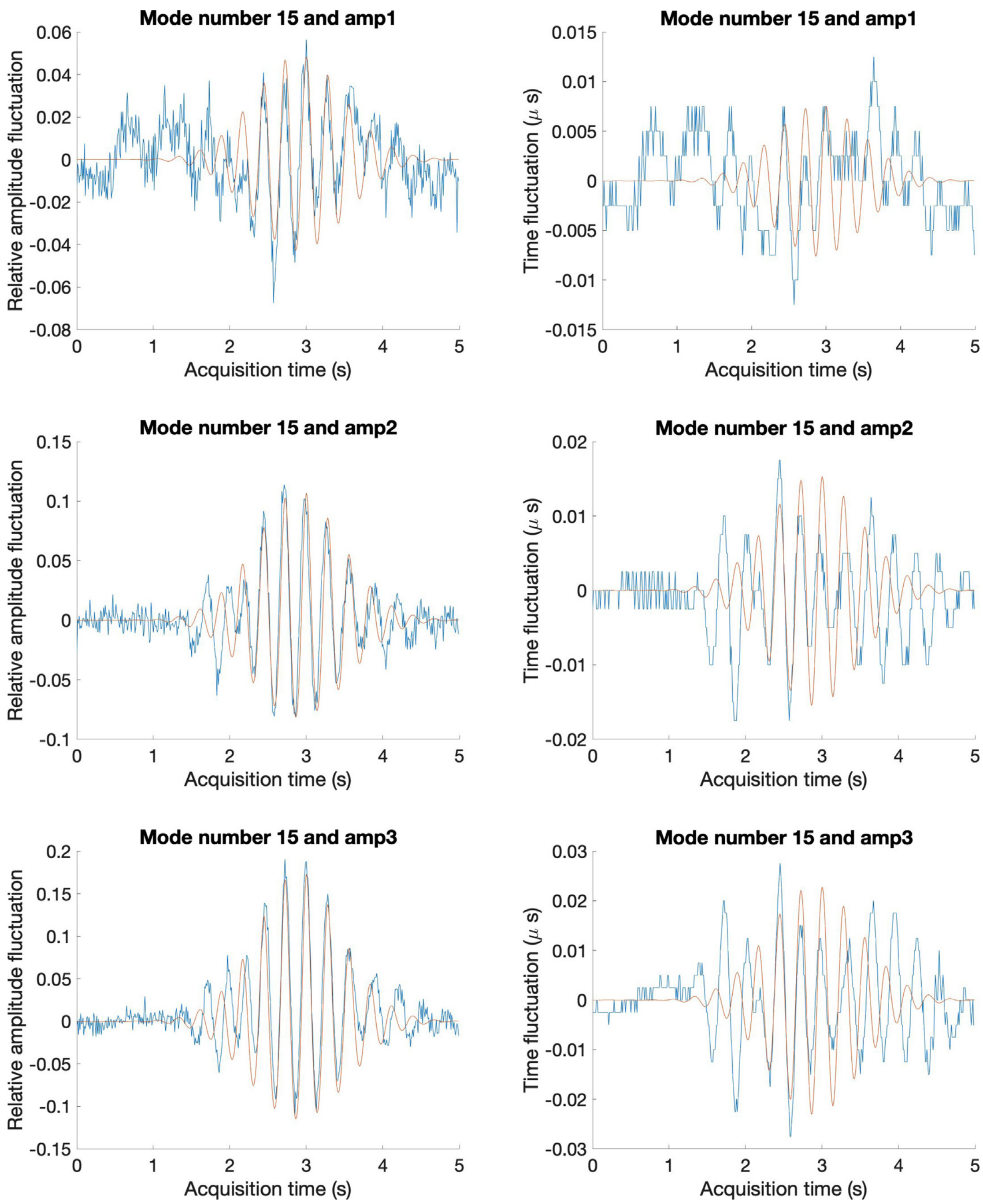

FIG. 3. (Color online) Relative amplitude and travel-time perturbations as functions of slow acquisition time for frequency $\omega_o = 2\pi \times 0.5 \times 10^6$ rad·s^{-1} and mode number 15 and for different surface perturbation amplitudes amp1, amp2, and amp3. The blue lines plot the experimental results. The red lines plot the theoretical results obtained from Eqs. (26) and (27).

agreement with the different voltages used to create the surface perturbations. We find $p_2 = 22.5\ \mathrm{s}^{-1}$ and $p_3 = 0.85^2\ \mathrm{s}^{-2}$, which correspond, respectively, to a central frequency $\nu = 22.5/(2\pi) \simeq 3.5$ Hz and a root mean square (rms) pulse width of 0.6 s, which is in agreement with the pulse generated by the shaker. Indeed, the pulse shape generated by the shaker has a carrier frequency equal to $\nu_{\mathrm{sh}} = 3.5$ Hz and a rms pulse width of $t_{\mathrm{sh}} = 0.25$ s. The capillary-gravity waves are dispersive with dispersion relation $\omega^2 \simeq (gk + (\sigma/\rho)k^3)$, where $g \simeq 9.8\ \mathrm{m/s}^2$ is the acceleration of gravity, $\sigma = 0.074$ N/m is the air–water surface tension, and $\rho = 1000\,\mathrm{kg/m}^3$ is the water density. The rms pulse width after a propagation distance d is then close to $t_{\mathrm{sh}}\sqrt{1 + k''(\omega_{\mathrm{sh}})^2 d^2/t_{\mathrm{sh}}^4}$, with $\omega_{\mathrm{sh}} = 2\pi\nu_{\mathrm{sh}}$. Around the frequency ω_{sh}, we have $k(\omega) \simeq \omega^2/g$ and $k''(\omega) \simeq 2/g$, so the rms pulse width after a propagation distance d is actually close to $t_{\mathrm{sh}}\sqrt{1 + 4d^2/(g^2 t_{\mathrm{sh}}^4)}$, which is equal to 0.6 s for $d = 0.6$ m. This is the approximate distance between the shaker and the position of the capillary-gravity waves when the acoustic waves are transmitted. Finally, we can clearly observe the nonlinear shape of the relative mode amplitude perturbation for the strongest surface perturbation amp3, as predicted by the theory [Eq. (27)].

In Fig. 4, we report the averaged relative amplitude perturbation $\langle (A_j/A_{j_0} - 1)^2 \rangle$ and time perturbation $\langle (T_j - T_{j_0})^2 \rangle$ as a function of the mode number j. The ensemble average $\langle\rangle$ is performed on the 500 transfer matrix acquisitions, while the surface perturbation travels at the air–water interface. We compare this with the theoretical forms [Eqs. (27) and (26)] with a least-square fit for ν_0 and ν_2 [for instance, at frequency 1 MHz, we find $(\pi^2\nu_0)/(k_o^2\mathcal{D}^2 L) = 2\,10^{-5}$ and $(\pi\nu_2 L_1(L - L_1))/(k_o\mathcal{D}^2 L^2) = 3\,10^{-4}$]. The dependence with respect to mode number is well predicted by the theory for both amplitude and time perturbations: the theory predicts a quadratic form for the time perturbation and a nearly quadratic form for the amplitude perturbation. The dependence with respect to carrier frequency ω_o is qualitatively predicted by the theory as the perturbations decay with increasing frequency. The dependence with respect to the surface perturbation amplitude is as expected, with relative amplitude and travel-time perturbations increasing linearly with surface perturbation amplitude.

VI. INVERSION OF THE SURFACE PERTURBATION FROM THE PARAXIAL APPROXIMATION

In this section, we aim to invert the surface perturbation at every point x between the two arrays (from $x = 0$ to $x = L$) through the paraxial approximation formulation. We recall that the paraxial regime holds when the typical wavelength λ_o is much smaller than the propagation distance L and the amplitude of the surface perturbation is small, with a scale of variation that is between λ_o and L. We expand the surface perturbation $\mu(x, y)$ as in Eq. (21) for all $y \in \left(-\sqrt{L\lambda_o}, \sqrt{L\lambda_o}\right)$. As shown in Appendix A 3, the expressions of the modal amplitudes of the pressure field after propagation between the two arrays in the paraxial single-scattering regime can be written as follows:

$$\hat{a}_j(\omega, L, 0) = A_{j,o}(\omega, L) + A_j^{per}(\omega, L), \tag{29}$$

$$A_j^{per}(\omega, L) = \sum_{l=1}^{N(\omega)} \frac{e^{3i\pi/4}}{4\sqrt{2\pi\beta_j\beta_l(\omega)}} \times \int_0^L \frac{\mu_0(x) e^{i(\beta_l(\omega) - \beta_j(\omega))x}}{\sqrt{\beta_j(\omega)x + \beta_l(\omega)(L - x)}} dx\, s_{jl} \hat{f}_l(\omega), \tag{30}$$

where $A_{j,o}(\omega, L)$ is the unperturbed amplitude of the jth mode [Eq. (16)], and the s_{jl} coefficients for every modal pair (j, l) are defined by

$$s_{jl} = 2\frac{\pi^2}{\mathcal{D}^2}(-1)^{l-j}\left(l - \frac{1}{2}\right)\left(j - \frac{1}{2}\right). \tag{31}$$

The term $A_j^{per}(\omega, L)$ in Eq. (30) is the perturbed mode amplitude due to the surface perturbation in the paraxial single-scattering regime. In Eqs. (29) and (30), we have neglected some terms that appear in Eq. (22) and that describe the mode amplitude perturbations [the terms associated with μ_2 in Eq. (21)], while we have kept the leading-order mode conversion terms that are the ones that are exploited in the resolution of the inverse problem.

In the following, we build a modal-based method to image the surface perturbation from the observation of the modal transmission matrix from the source array to the receiver array. We anticipate that it is difficult in practice to extract all modes from the signals recorded by the source–receiver arrays, so we assume that we can only extract the first M modes from the wave field, with $M \in \{1, \ldots, N\}$.

Equations (29) and (30) give the forward model $\mathcal{F}$ that determines the modal transmission matrix $(T_{jl}(\omega))_{j,l=1}^M$ from the surface perturbation $(\mu_0(x))_{x\in(0,L)}$, where $T_{jl}(\omega)$ is the complex amplitude of the jth perturbed modal amplitude $A_j^{per}(\omega, L)$ seen by the receiver array when the source transmits a unit-amplitude lth mode (the source is such that $\hat{f}_{l'} = 0$ for $l' \neq l$ and $\hat{f}_l = 1$). According to Eq. (30), the forward model has the form $\mathcal{F} : (\mu_0(x))_{x\in(0,L)} \mapsto (T_{jl})_{j,l=1}^M$ with

$$T_{jl} = \mathcal{F}[\mu_0]_{jl} = \frac{e^{3i\pi/4} s_{jl}}{4\sqrt{2\pi\beta_j\beta_l}} \int_0^L \frac{\mu_0(x) e^{i(\beta_l - \beta_j)x}}{\sqrt{\beta_j x + \beta_l(L - x)}} dx, \quad j, l = 1, \ldots, M. \tag{32}$$

The adjoint operator has the form $\mathcal{F}^* : (T_{jl})_{j,l=1}^M \mapsto (\mu_0(x))_{x\in(0,L)}$ with

$$\mu_0(x) = \mathcal{F}^*[T](x) = \sum_{j,l=1}^M \frac{e^{-3i\pi/4} s_{jl}}{4\sqrt{2\pi\beta_j\beta_l}} \frac{T_{jl} e^{-i(\beta_l - \beta_j)x}}{\sqrt{\beta_j x + \beta_l(L - x)}}, \quad x \in (0, L). \tag{33}$$

We can then deduce that the normal operator $\mathcal{F}^*\mathcal{F}$ has the form

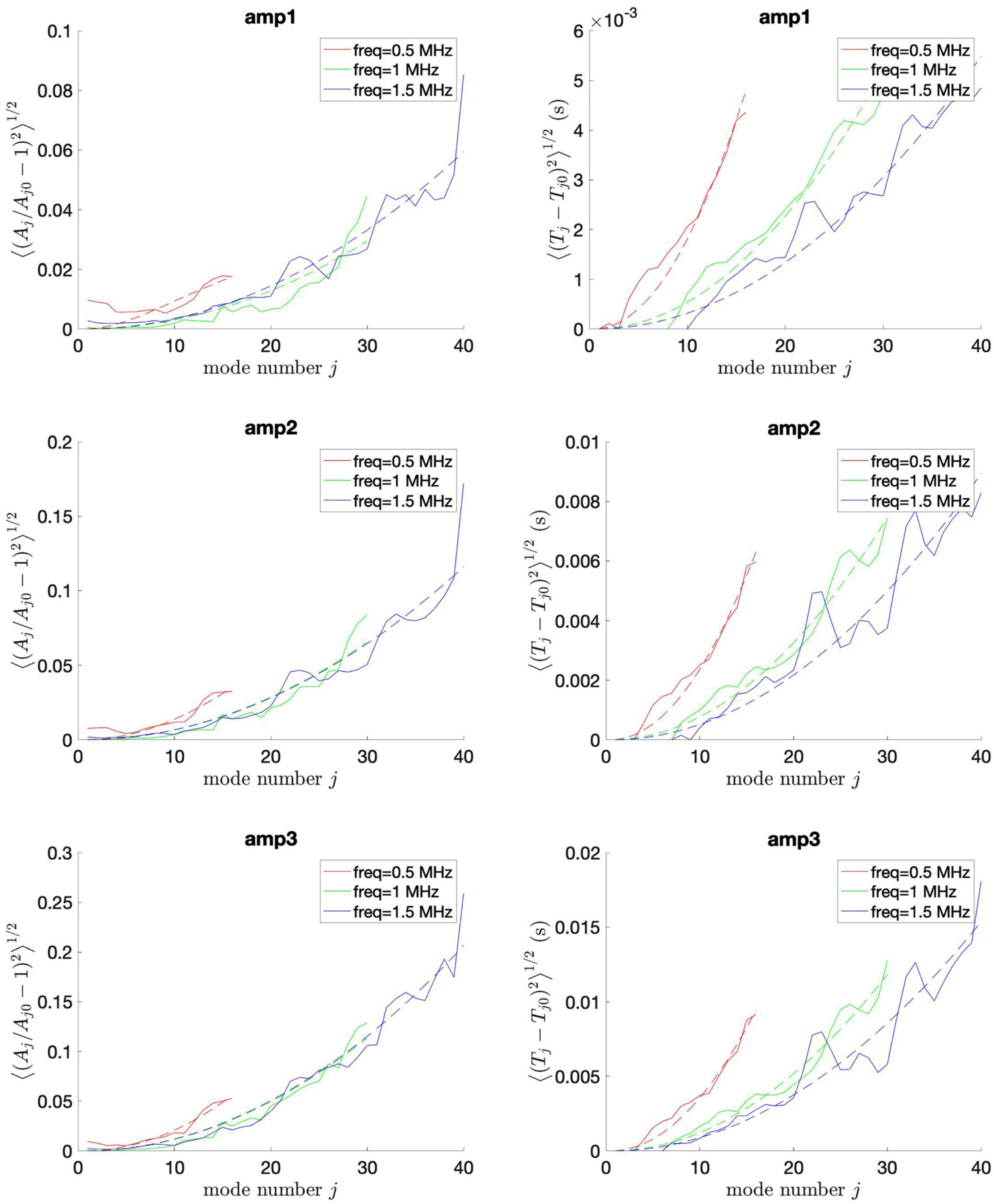

FIG. 4. (Color online) Relative amplitude and travel-time perturbations as functions of mode number for different carrier frequencies ω_o and for different surface perturbation amplitudes amp1, amp2, and amp3. The solid lines plot the experimental results. The dashed lines plot the theoretical results obtained from Eqs. (26) and (27).

$$\mathcal{F}^*\mathcal{F}[\mu_0](x) = \int_0^L a_{\mathcal{F}}(x,x')\mu_0(x')dx', \quad x \in (0,L), \tag{34}$$

with the kernel $a_{\mathcal{F}}$ given by

$$a_{\mathcal{F}}(x,x') = \sum_{j,l=1}^{M} \frac{s_{jl}^2}{32\pi\beta_j\beta_l} \times \frac{e^{i(\beta_l-\beta_j)(x'-x)}}{\sqrt{\beta_j x + \beta_l(L-x)}\sqrt{\beta_j x' + \beta_l(L-x')}}. \tag{35}$$

The inverse problem that consists in recovering the surface perturbation $(\mu_0(x))_{x\in(0,L)}$ from the observed transmission matrix $(T_{jl})_{j,l=1}^M$ can be solved using a pseudo-inverse or a regularized inverse approach. The estimated surface perturbation is then $(\mathcal{F}^*\mathcal{F} + \gamma\mathcal{I})^{-1}\mathcal{F}^*[T]$ for some regularization parameter $\gamma > 0$. Indeed, according to Lemma C in Appendix B 4, the kernel of the normal operator is almost a convolution kernel concentrated on the diagonal $x' = x$, which shows that the normal operator is close to the identity up to a multiplicative constant: $\mathcal{F}^*\mathcal{F}[\mu_0](x) \approx \mu_0(x)$. Therefore, the pseudo-inverse or regularized inverse is close to the adjoint operator (up to a multiplicative constant). We can also use an approximate inverse that is close to the adjoint operator and that has a physical interpretation as explained below.

We define the imaging function $\mathcal{I}$ in terms of the measured transmission matrix $(T_{jl})_{j,l=1}^{M}$ as

$$\mathcal{I}(x_0) = \sum_{j,l=1}^{M} \frac{T_{jl} e^{-3i\pi/4} (-1)^{j-l} \sqrt{\beta_j \beta_l}}{\left(j-\frac{1}{2}\right)\left(l-\frac{1}{2}\right)} e^{-i(\beta_l-\beta_j)x_0}, \quad x_o \in (0, L). \tag{36}$$

The imaging function [Eq. (36)] is close to the adjoint operator $\mathcal{F}^*$ applied to the measured transmission matrix, as can be seen by a comparison of Eq. (36) with the expression of Eq. (33) of the adjoint operator: the phase factors are equal; the differences are only in the amplitudes. It is possible to interpret the imaging function Eq. (36) as a DBF process in the modal domain. To clarify this, let us fix $x_0 \in (0, L)$, and let us consider a source function with the following modal coefficients:

$$\hat{f}_l = \frac{(-1)^l \sqrt{\beta_l} e^{-3i\pi/4}}{l-\frac{1}{2}} e^{-i\beta_l x_0} \quad \text{for } l \le M. \tag{37}$$

Given the perturbed modal amplitudes $(A_j^{per})_{j=1}^{M}$ of the wave signals recorded by the receiver array and transmitted by the source [Eq. (37)], the imaging function [Eq. (36)] can be expressed as

$$\mathcal{I}(x_0) = \sum_{j=1}^{M} A_j^{per} \frac{(-1)^j \sqrt{\beta_j}}{j-\frac{1}{2}} e^{i\beta_j x_0}. \tag{38}$$

This representation of the imaging function is obtained by substituting the expression

$$A_j^{per} = \sum_{l=1}^{M} T_{jl} \hat{f}_l$$

into the definition [Eq. (36)] of the imaging function, with $\hat{f}_l$ given by Eq. (37) and $(T_{jl})_{j,l=1}^{M}$ being the measured transmission matrix. The representation of Eq. (38) of the imaging function makes it possible to explain the analogy with a DBF process.

Indeed, the source [Eq. (37)] is designed to produce a focal spot centered at the point $(x_0, 0, \mathcal{D})$. When $\alpha = M/N$ is equal to one, the size of the focal spot is diffraction-limited, and its radius is on the order of the wavelength. When $\alpha = M/N$ is small, the focal spot is on the order of the wavelength divided by α in the depth direction z and on the order of the wavelength divided by α^2 in the range direction x (see Appendix B 2 for details).

The imaging process, therefore, looks like a DBF process as beamforming is performed here both from modal projection in transmission by Eq. (37) and in reception by Eq. (38). We can then anticipate the extraction of local information on the surface perturbation around $(x_0, 0, \mathcal{D})$ by this formulation in a way equivalent to what was performed for DBF eigenbeam selection applied to source–receiver (sub)arrays in the sensitivity kernel (SK) approach.[4,10,13,16]

It follows that the imaging function gives an image of the surface perturbation $\mu_0(x)$, and it is possible to quantify its resolution properties. As shown in Appendix B 3, when $\alpha = M/N \ll 1$, we have

$$\mathcal{I}(x_0) = \int_0^L \mathcal{K}(x_0 - x)\mu_0(x)dx, \tag{39}$$

where $\mathcal{K}(x) = (k^{3/2}\alpha^2)/\left(2\sqrt{2\pi L}\right)|\psi(\alpha^2 kx)|^2$ and $\psi(x) = \sqrt{2} \times \left(C\left(x/\sqrt{2}\right) - iS\left(x/\sqrt{2}\right)\right)/x$, with C and S as Fresnel integrals $C(x) = \int_0^x \cos(s^2)ds$, $S(x) = \int_0^x \sin(s^2)ds$, and $k = \omega/c$.

Note that the inversion kernel $\mathcal{K}(x)$ is integrable (it decays as x^{-2}), so the imaging function $\mathcal{I}(x_0)$ gives a smoothed image of the surface perturbation $\mu_0(x_0)$ with a resolution on the order of the wavelength divided by α^2. More exactly, the half-width at half-maximum of $|\psi|^2$ is approximately equal to 2, so the resolution is $\simeq \lambda_o/(\pi\alpha^2)$. Of course, the more modes we can extract from the data, the better the resolution is, and we could ultimately reach resolution on the order of the wavelength if we could exploit the amplitudes of all of the propagative modes with indices up to $j = N$. We also have $\int_{\mathbb{R}} \mathcal{K}(x)dx = \pi\sqrt{k}/(2\sqrt{2L})$, which makes it possible to estimate $\mu_0(x_0) \simeq \left[\left(2\sqrt{2L}\right)/(\pi\sqrt{k})\right]\mathcal{I}(x_0)$ when it is varying slowly.

The imaging function of Eq. (36) uses only the data recorded at one frequency. For broadband data, it is straightforward to sum the time-harmonic imaging functions over the available frequency band. In the following example, we sum over 40 frequencies regularly spaced in the band $[0.8, 1.2]$ MHz.

In Figs. 5 and 6, we compare the modal-based imaging function [Eq. (36)] with the DBF eigenbeam inversion applied on the same experimental data (EXP1 and EXP2) in Refs. 4 and 13. In the modal-based approach, the number of modes is approximately $N = 70$ ($N = 58$ at 0.8 MHz and $N = 88$ at 1.2 MHz), and $M = 20$ modes can be exploited in the band $[0.8, 1.2]$ MHz (i.e., $\alpha \simeq 0.3$). The resolution is, therefore, on the order of half a centimeter, which is smaller than the capillary-gravity wavelength of the surface perturbation.

In Ref. 4, a one-dimensional SK formulation was proposed to invert for both amplitude and travel-time fluctuations for a complete set of DBF eigenbeams. The inversion leads to a maximum volume perturbation estimation of $\Delta V = 22\,\text{mm}^3$. This volume is difficult to interpret in terms of surface elevation, as the lateral extent of the Fresnel zone was not taken into account in the computation of the surface SK. In other words, the inversion result projected along the source–receiver axis should have been weighted by the lateral extent of the SK along the direction perpendicular to the waveguide. This problem is solved in the present paraxial approximation, where the three-dimensional aspect of the propagation projected on the surface perturbation is

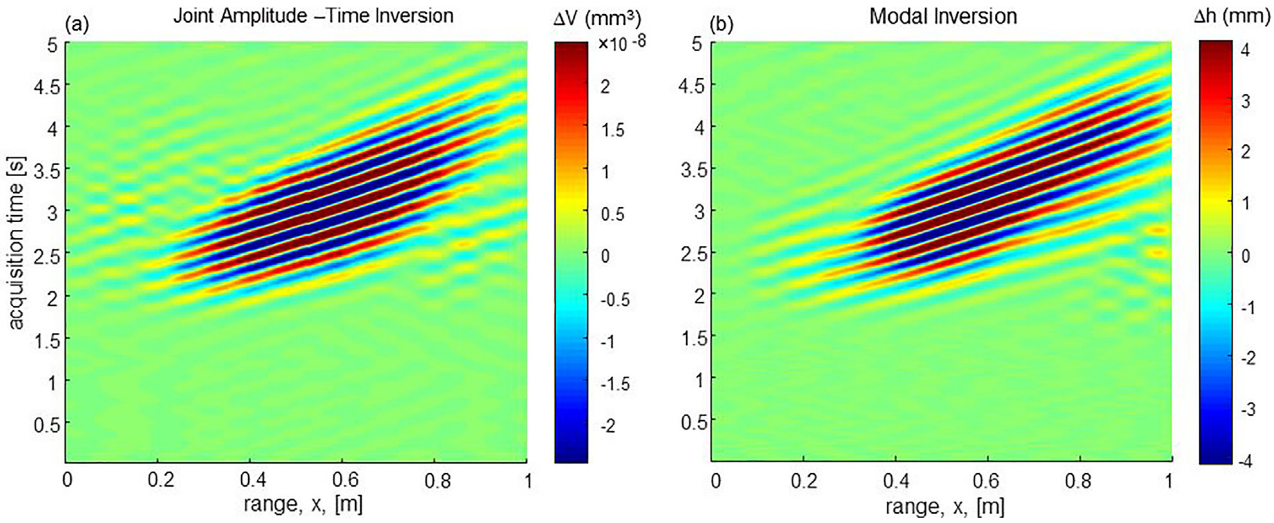

FIG. 5. (Color online) Estimation of the surface perturbation in the experimental configuration EXP1. (a) The DBF approach (Ref. 4) performed from a joint inversion of both amplitudes and times of a set of more than 2000 eigenbeams. Using a one-dimensional SK, the inversion is plotted as a function of the volume ΔV of the perturbation. (b) The modal-based approach described in the present paper with the surface deformation $\Delta h(x) = \mathcal{D}\mu_0(x)$ shown in mm.

taken into account in the forward problem. The inversion result in Fig. 5(a) shows a maximum 3-mm surface deformation along the source–receiver axis that is consistent with external observations.

In Refs. 13 and 14, two-dimensional surface SKs applied to DBF eigenbeams were used for amplitude, travel-time, or emitting-receiving angle perturbations that lead to surface elevation estimations on the order of 20 μm for weak laser excitation and up to 2 mm for strong laser excitation. The optimal inversion result obtained so far was for a joint angle inversion on emitting-receiving angle perturbations for a set of more than 2000 eigenbeams and very weak laser excitation [Fig. 6(a)]. Interestingly enough, the modal projection used within the paraxial approximation in the present paper did not extract the modal transmission matrix above the noise level in the case of this very weak laser excitation. For stronger laser excitation, the inversion result obtained from the paraxial approximation in Fig. 6(b) shows a similar shape for the two counter-propagative gravity-capillary waves generated from the center of the waveguide, with a maximum 0.5-mm surface elevation.

When comparing the eigenbeam approach and the modal transmission matrix approach to invert for an unknown surface deformation in an acoustic waveguide, we should keep in mind the following points. First, extracting the complete set of eigenbeams between the transmitting and receiving (sub)arrays via a DBF algorithm is much more time consuming than extracting the modal transmission matrix as proposed here in the paraxial approximation formulation. However, as discussed in Ref. 14, only the independent families of eigenbeams would be worth extracting via DBF, which could greatly reduce the computational time under the eigenbeam approach. Second, it appears from experimental investigations that the fluctuations of the modal transmission matrix are sensitive to surface deformation elevation on the order of a wavelength when the eigenbeam amplitude fluctuations are sensitive to elevation that can be 10 times weaker. Finally, the eigenbeam algorithm applied to sub-antennas on both sides of the waveguide does not require the transmitting and receiving arrays to cover the entire water column, which can have significant advantages in ocean experiments. The mode-based imaging method proposed here in the paraxial approximation requires extraction of modal amplitudes that can be estimated by a simple projection when the antenna array is dense and covers the cross section of the waveguide. When the antenna array covers only a limited portion of the cross section, it is still possible to extract the first modal amplitudes from the wave signals recorded by the receiver array by using an appropriate weighted projection method, provided that we know the mode profiles and the modal wavenumbers, as explained in Refs. 17 and 18. This method works as long as the array aperture is not too small compared to the waveguide depth.

VII. CONCLUSION

In conclusion, we recall the main results of the present study: (1) we propose a formulation based on the paraxial approximation in the context of an acoustic waveguide to describe both three-dimensional aspects of the forward propagation and the interaction with a complex surface deformation; (2) the prediction of the wavefield projected onto the mode profiles between two source–receiver arrays provides an explanation for the nonlinear shape of modal amplitude fluctuations that was experimentally observed, but up until now not understood, in the presence of strong surface deformation; (3) within the paraxial approximation, the formulation of the inverse problem is proposed to obtain the surface deformation at any position between the source–receiver arrays from the observed modal transmission matrix; (4) when applied to experimental tank data in an ultrasonic waveguide, excellent agreement is observed with a different

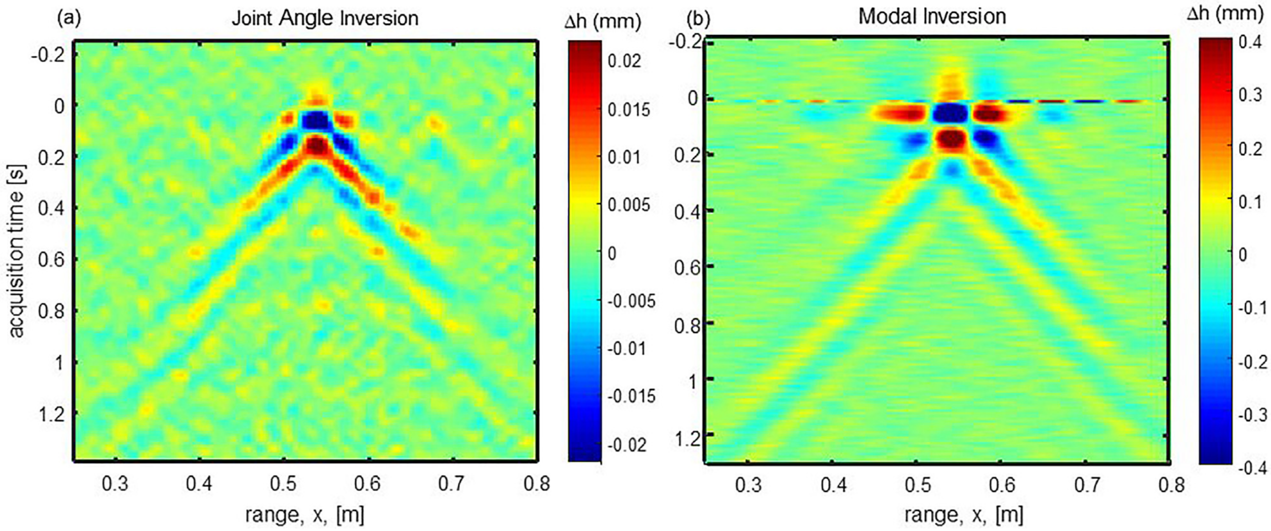

FIG. 6. (Color online) Estimation of the surface perturbation in the experimental configuration EXP2. (a) The DBF approach (Ref. 13) performed from a joint inversion of both source and receive angles of a set of more than 2000 eigenbeams and a two-dimensional SK. (b) The modal-based approach described in the present paper with the surface deformation $\Delta h(x) = \mathcal{D}\mu_0(x)$. Both inversions in (a) and (b) are plotted in mm. However, the joint angle inversion was performed from a dataset induced from weak laser excitation (inducing low values of Δh) when the modal inversion was achieved from stronger laser excitation at the air–water interface, with maximum Δh values on the order of 1 mm.

inversion algorithm that was proposed recently through eigenbeam selection in the framework of the SK approach.

ACKNOWLEDGMENTS

The authors wish to thank Tobias Van Baarsel for technical help in the design of some of the figures. ISTerre is part of Labex OSUG@2020 (ANR10 LABX56). The work of JG is supported by the French Agence Nationale de la Recherche (ANR) under Grant No. ANR-19-CE46-0007 (project ICCI).

APPENDIX A: PARAXIAL APPROXIMATION

The first steps of the analysis follow the lines of that in Ref. 19, which is itself based on the modal approach introduced and studied in Refs. 20–25.

1. Change of coordinates

Consider the change of coordinates from (x, y, z) to (x, y, η), with

$$\eta = \frac{z\mathcal{D}}{T(x,y)}, \tag{A1}$$

which straightens the boundary $z = T(x,y)$ to $\eta = \mathcal{D}$ for any $(x,y) \in \mathbb{R}^2$. The pressure field in the new coordinates is given by

$$\hat{P}(\omega,x,y,\eta) = \hat{p}\left(\omega,x,y,\frac{\eta T(x,y)}{\mathcal{D}}\right). \tag{A2}$$

This satisfies the simple boundary conditions

$$\hat{P}(\omega,x,y,\mathcal{D}) = \partial_\eta \hat{P}(\omega,x,y,0) = 0 \tag{A3}$$

and the partial differential equation

$$\left[\partial_x^2 + \partial_y^2 + \left(\frac{\mathcal{D}^2}{T^2} + \eta^2\frac{|\nabla T|^2}{T^2}\right)\partial_\eta^2 - 2\eta\frac{\nabla T}{T}\cdot\nabla\partial_\eta + \left(2\eta\frac{|\nabla T|^2}{T^2} - \eta\frac{\Delta T}{T}\right)\partial_\eta + k^2\right]\hat{P} = \hat{f}(\omega,\eta)\delta(x)\delta(y), \tag{A4}$$

derived from Eqs. (1) and (A2) using the chain rule. Here, ∇ and Δ are the gradient and Laplacian operators in (x, y). When substituting the model of Eq. (2) into Eq. (A4), we obtain that $\hat{P}$ satisfies a perturbed problem

$$\left[\partial_x^2 + \partial_y^2 + \partial_\eta^2 + k^2 + p.t.\right]\hat{P}(\omega,x,y,\eta) = \hat{f}(\omega,\eta)\delta(x)\delta(y), \tag{A5}$$

where the perturbed terms $p.t.$ are

$$p.t. = r_1(x,y,\eta)\partial_\eta^2 + r_2(x,y,\eta)\partial_{\eta x}^2 + r_3(x,y,\eta)\partial_{\eta y}^2 + r_4(x,y,\eta)\partial_\eta,$$

with functions

$$r_1(x,y,\eta) = -\frac{2\mu+\mu^2}{(1+\mu)^2} + \eta^2\frac{(\partial_x\mu)^2 + (\partial_y\mu)^2}{(1+\mu)^2},$$

$$r_2(x,y,\eta) = -2\eta\frac{\partial_x\mu}{1+\mu},$$

$$r_3(x,y,\eta) = -2\eta\frac{\partial_y\mu}{1+\mu},$$

$$r_4(x,y,\eta) = 2\eta\frac{(\partial_x\mu)^2 + (\partial_y\mu)^2}{(1+\mu)^2} - \eta\frac{\partial_x^2\mu + \partial_y^2\mu}{1+\mu}.$$

2. Wave decomposition

Equation (A5) is not separable, but we can still write its solution on the basis of the eigenfunctions of Eq. (4) of the unperturbed waveguide because the basis is complete. The expansion has the general form

$$\hat{P}(\omega,x,y,\eta) = \sum_{j=1}^{N(\omega)} \phi_j(\eta)\hat{u}_j(\omega,x,y) + \sum_{j>N(\omega)} \phi_j(\eta)\hat{v}_j(\omega,x,y). \tag{A6}$$

We define the forward and backward going wave modal amplitudes $\hat{a}_j$ and $\hat{b}_j$ by

$$\hat{a}_j(\omega,x,y) = \left(\frac{1}{2}\hat{u}_j(\omega,x,y) + \frac{1}{2i\beta_j(\omega)}\partial_x\hat{u}_j(\omega,x,y)\right)e^{-i\beta_j(\omega)x}, \tag{A7}$$

$$\hat{b}_j(\omega,x,y) = \left(\frac{1}{2}\hat{u}_j(\omega,x,y) - \frac{1}{2i\beta_j(\omega)}\partial_x\hat{u}_j(\omega,x,y)\right)e^{i\beta_j(\omega)x}, \tag{A8}$$

so that the complex-valued amplitudes of the propagative modes can be written as

$$\hat{u}_j(\omega,x,y) = \hat{a}_j(\omega,x,y)e^{i\beta_j(\omega)x} + \hat{b}_j(\omega,x,y)e^{-i\beta_j(\omega)x}. \tag{A9}$$

The modal amplitudes of the propagative modes each satisfy a boundary condition in the range $(0,L)$ of the surface fluctuations. To derive these boundary conditions, we first observe that because the boundary is flat outside $(0,L)$, the radiation (outgoing conditions) implies that the modal amplitudes satisfy

$$\hat{a}_j(\omega,x=0^-,y) = 0, \quad \hat{b}_j(\omega,x=L,y) = 0. \tag{A10}$$

This last equation is the boundary condition for $\hat{b}_j$. The boundary value $\hat{a}_j(\omega,x=0^+,y)$ follows from the jump conditions across the plane $x=0$ due to the source in Eq. (A5). We have $[\hat{u}_j]_{0^-}^{0^+} = 0$, $[\partial_x\hat{u}_j]_{0^-}^{0^+} = \hat{f}_j(\omega)\delta(y)$, with $\hat{f}_j$ defined by Eq. (7). This gives $[\hat{a}_j + \hat{b}_j]_{0^-}^{0^+} = 0$, $i\beta_j[\hat{a}_j - \hat{b}_j]_{0^-}^{0^+} = \hat{f}_j(\omega) \times\delta(y)$ and therefore

$$\hat{a}_j(\omega,0^+,y) = \frac{\hat{f}_j(\omega)}{2i\beta_j(\omega)}\delta(y). \tag{A11}$$

Substituting Eq. (A6) into Eq. (A5), using the orthonormality of the eigenfunctions ϕ_j and the relation $\partial_x\hat{a}_j(\omega,x,y) e^{i\beta_j(\omega)x} + \partial_x\hat{b}_j(\omega,x,y)e^{-i\beta_j(\omega)x} = 0$ that comes from Eqs. (A7) and (A8), we find that the modal amplitudes solve paraxial equations coupled by the surface fluctuations in $z \in (0,L)$,

$$\left(2i\beta_j\partial_x + \partial_y^2\right)\hat{a}_j + e^{-2i\beta_j x}\partial_y^2\hat{b}_j = \mathcal{E}_{j,\mathbf{a}}(\hat{\mathbf{a}},\hat{\mathbf{b}},\hat{\mathbf{v}},x,y), \tag{A12}$$

$$\left(-2i\beta_j\partial_x + \partial_y^2\right)\hat{b}_j + e^{2i\beta_j x}\partial_y^2\hat{a}_j = \mathcal{E}_{j,\mathbf{b}}(\hat{\mathbf{a}},\hat{\mathbf{b}},\hat{\mathbf{v}},x,y), \tag{A13}$$

with the coupled terms given by

$$\begin{aligned}
&\mathcal{E}_{j,\mathbf{a}}(\hat{\mathbf{a}},\hat{\mathbf{b}},\hat{\mathbf{v}},x,y)\\
&= -\sum_{l=1}^{N} e^{i(\beta_l-\beta_j)x}\left[r_{jl}^1(x,y)\hat{a}_l + i\beta_l r_{jl}^2(x,y)\hat{a}_l + r_{jl}^3(x,y)\partial_y\hat{a}_l\right]\\
&\quad -\sum_{l=1}^{N} e^{i(-\beta_l-\beta_j)x}\left[r_{jl}^1(x,y)\hat{b}_l - i\beta_l r_{jl}^2(x,y)\hat{b}_l + r_{jl}^3(x,y)\partial_y\hat{b}_l\right]\\
&\quad -\sum_{l>N} e^{-i\beta_j x}\left[r_{jl}^1(x,y)\hat{v}_l + r_{jl}^2(x,y)\partial_x\hat{v}_l + r_{jl}^3(x,y)\partial_y\hat{v}_l\right],\\
&\mathcal{E}_{j,\mathbf{b}}(\hat{\mathbf{a}},\hat{\mathbf{b}},\hat{\mathbf{v}},x,y)\\
&= -\sum_{l=1}^{N} e^{i(\beta_l+\beta_j)x}\left[r_{jl}^1(x,y)\hat{a}_l + i\beta_l r_{jl}^2(x,y)\hat{a}_l + r_{jl}^3(x,y)\partial_y\hat{a}_l\right]\\
&\quad -\sum_{l=1}^{N} e^{i(-\beta_l+\beta_j)x}\left[r_{jl}^1(x,y)\hat{b}_l - i\beta_l r_{jl}^2(x,y)\hat{b}_l + r_{jl}^3(x,y)\partial_y\hat{b}_l\right]\\
&\quad -\sum_{l>N} e^{i\beta_j x}\left[r_{jl}^1(x,y)\hat{v}_l + r_{jl}^2(x,y)\partial_x\hat{v}_l + r_{jl}^3(x,y)\partial_y\hat{v}_l\right],
\end{aligned}$$

in terms of

$$\begin{aligned}
r_{jl}^1(x,y) &= \int_0^{\mathcal{D}} d\eta\left[\phi_j(\eta)\phi_l''(\eta)r_1(x,y,\eta) + \phi_j(\eta)\phi_l'(\eta)r_4(x,y,\eta)\right],\\
r_{jl}^2(x,y) &= \int_0^{\mathcal{D}} d\eta\,\phi_j(\eta)\phi_l'(\eta)r_2(x,y,\eta),\\
r_{jl}^3(x,y) &= \int_0^{\mathcal{D}} d\eta\,\phi_j(\eta)\phi_l'(\eta)r_3(x,y,\eta).
\end{aligned}$$

The equations for the evanescent components are obtained similarly,

$$\left(\partial_x^2 + \partial_y^2 - \beta_j^2\right)\hat{v}_j = \mathcal{E}_{j,\mathbf{v}}(\hat{\mathbf{a}},\hat{\mathbf{b}},\hat{\mathbf{v}},x,y), \tag{A14}$$

with the coupled term $\mathcal{E}_{j,\mathbf{v}}(\hat{\mathbf{a}},\hat{\mathbf{b}},\hat{\mathbf{v}},x,y)$ as in Eqs. (A12) and (A13), and they are augmented with the decay conditions $\hat{v}_j(\omega,x,y) \to 0$ as $\sqrt{x^2+y^2} \to \infty$ for all $j \geq N+1$. The equations for the modal amplitudes of the evanescent modes are similar to those encountered in Ref. 26. These amplitudes were shown to vanish in Ref. 26 (Sec. 3.3) in a regime that was similar to the one addressed in this paper. We therefore neglect them in the following.

From Eqs. (A12) and (A13), we obtain that the modal amplitudes of the propagative modes satisfy the system of partial differential equations

$$\begin{aligned}
&\begin{pmatrix} 2i\beta_j\partial_x + \partial_y^2 & e^{-2i\beta_j x}\partial_y^2 \\ e^{2i\beta_j x}\partial_y^2 & -2i\beta_j\partial_x + \partial_y^2 \end{pmatrix}\begin{pmatrix}\hat{a}_j\\ \hat{b}_j\end{pmatrix}\\
&= -\sum_{l=1}^{N}\begin{pmatrix} e^{-i(\beta_j-\beta_l)x} & e^{-i(\beta_j+\beta_l)x} \\ e^{i(\beta_j+\beta_l)x} & e^{i(\beta_j-\beta_l)x}\end{pmatrix}\left[r_{jl}^1(x,y) + r_{jl}^3(x,y)\partial_y\right]\begin{pmatrix}\hat{a}_l\\ \hat{b}_l\end{pmatrix}\\
&\quad -\sum_{l=1}^{N} i\beta_l r_{jl}^2(x,y)\begin{pmatrix} e^{-i(\beta_j-\beta_l)x} & -e^{-i(\beta_j+\beta_l)x} \\ e^{i(\beta_j+\beta_l)x} & -e^{i(\beta_j-\beta_l)x}\end{pmatrix}\begin{pmatrix}\hat{a}_l\\ \hat{b}_l\end{pmatrix}
\end{aligned} \tag{A15}$$

for $j = 1,\ldots,N$ with initial and end conditions

https://doi.org/10.1121/10.0010533

$$\hat{a}_j(\omega,0,y) = \frac{\hat{f}_j(\omega)}{2i\beta_j(\omega)}\delta(y), \quad \hat{b}_j(\omega,L,y) = 0. \qquad \text{(A16)}$$

If we apply the multi-scale analysis proposed in Ref. 12 in the paraxial regime, then we get Eq. (18), which gives the leading-order perturbations of the modal amplitudes generated by the surface perturbation μ. In Appendix A 3, we present a detailed approach that makes it possible to capture all of the terms that are linear in the surface perturbation μ.

3. Time-harmonic single-scattering wave propagation in the paraxial regime

In this subsection, we prove Eq. (29). We only keep the terms linear in μ and neglect the backscattered wave components $\hat{b}_j$ in Eq. (A15). We simplify the notations and do not write the ω-dependence explicitly. This gives the following coupled paraxial wave equations for the modal amplitudes $\hat{a}_j$:

$$\begin{aligned}&\left[2i\beta_j\partial_x + \partial_y^2\right]\hat{a}_j\\ &\quad = \mu(x,y)\sum_{l=1}^N q_{jl}e^{i(\beta_l-\beta_j)x}\hat{a}_l + (\partial_x^2+\partial_y^2)\mu(x,y)\\ &\qquad \times \sum_{l=1}^N r_{jl}e^{i(\beta_l-\beta_j)x}\hat{a}_l + \partial_y\mu(x,y)\sum_{l=1}^N 2r_{jl}e^{i(\beta_l-\beta_j)x}\partial_y\hat{a}_l\\ &\qquad + \partial_x\mu(x,y)\sum_{l=1}^N 2r_{jl}e^{i(\beta_l-\beta_j)x}i\beta_l\hat{a}_l, \qquad \text{(A17)}\end{aligned}$$

where

$$q_{jl} = 2\int_0^{\mathcal{D}} d\eta\,\phi_j(\eta)\phi_l''(\eta) = -2\left(\frac{\pi}{\mathcal{D}}\right)^2\left(j-\frac{1}{2}\right)^2\delta_{jl}, \qquad \text{(A18)}$$

$$\begin{aligned}r_{jl} &= \int_0^{\mathcal{D}} d\eta\,\eta\,\phi_j(\eta)\phi_l'(\eta)\\ &= -\frac{1}{2}\delta_{jl} + \frac{2\left(l-\frac{1}{2}\right)\left(j-\frac{1}{2}\right)}{(l-j)(l+j-1)}(-1)^{l-j}(1-\delta_{jl}). \qquad \text{(A19)}\end{aligned}$$

We apply the single-scattering approximation, and we get

$$\begin{aligned}\hat{a}_j(L,0) &= \hat{G}(\beta_j,L,0)\hat{f}_j + \sum_{l=1}^N\int_0^L\int_{\mathbb{R}}\hat{G}(\beta_j,L-x,y)\\ &\quad\times\Big[\mu(x,y)q_{jl}\hat{G}(\beta_l,x,y)\\ &\quad + (\partial_x^2+\partial_y^2)\mu(x,y)r_{jl}\hat{G}(\beta_l,x,y)\\ &\quad + \partial_y\mu(x,y)2r_{jl}\partial_y\hat{G}(\beta_l,x,y)\\ &\quad + \partial_x\mu(x,y)2r_{jl}i\beta_l\hat{G}(\beta_l,x,y)\Big]e^{i(\beta_l-\beta_j)x}dydx\hat{f}_l, \qquad \text{(A20)}\end{aligned}$$

where $\hat{G}$ is the homogeneous paraxial Green's function,

$$\hat{G}(\beta,x,y) = \frac{e^{-3i\pi/4}}{2\sqrt{2\pi\beta x}}\exp\left(i\beta\frac{y^2}{2x}\right),$$

and we have used the fact that $\hat{G}(\beta,x,-y) = \hat{G}(\beta,x,y)$. After integration by parts, we find

$$\begin{aligned}\hat{a}_j(L,0) &= \hat{G}(\beta_j,L,0)\hat{f}_j + \int\int\hat{G}(\beta_j,L-x,y)\mu(x,y)\\ &\quad\times\hat{G}(\beta_j,x,y)dydxq_{jj}\hat{f}_j + \sum_{l=1}^N\int\int\hat{G}(\beta_j,L-x,y)\\ &\quad\times\mu(x,y)\hat{G}(\beta_l,x,y)dye^{i(\beta_l-\beta_j)x}dxr_{jl}(\beta_l^2-\beta_j^2)\hat{f}_l, \qquad \text{(A21)}\end{aligned}$$

up to terms that involve products of $\partial_y\mu$ and $\partial_y G$, which are smaller in the paraxial regime. Due to the form of the paraxial Green's function $\hat{G}$, the modal amplitude $\hat{a}_j$ is only sensitive to the perturbations $\mu(x,y)$ in a tube going from $(x=0,y=0)$ to $(x=L,y=0)$, with width $\sqrt{L\lambda_o}$. If $\mu(x,y)\simeq\mu_0(x)$ for all $y\in\left(-\sqrt{L\lambda_o},\sqrt{L\lambda_o}\right)$, then using

$$\begin{aligned}&\int\hat{G}(\beta_j,L-x,y)\hat{G}(\beta_l,x,y)dy\\ &\quad = -\frac{e^{3i\pi/4}}{4\sqrt{2\pi\beta_j\beta_l}\sqrt{\beta_j x+\beta_l(L-x)}},\end{aligned}$$

we get

$$\begin{aligned}\hat{a}_j(L,0) &= \frac{e^{-3i\pi/4}}{2\sqrt{2\pi\beta_j L}}\hat{f}_j - \frac{e^{3i\pi/4}}{4\sqrt{2\pi\beta_j^3 L}}\int_0^L\mu_0(x)dxq_{jj}\hat{f}_j\\ &\quad - \sum_{l=1}^N\frac{e^{3i\pi/4}}{4\sqrt{2\pi\beta_j\beta_l}}\int_0^L\frac{\mu_0(x)e^{i(\beta_l-\beta_j)x}}{\sqrt{\beta_j x+\beta_l(L-x)}}dx\\ &\quad\times r_{jl}(\beta_l^2-\beta_j^2)\hat{f}_l. \qquad \text{(A22)}\end{aligned}$$

We note that $r_{jl}(\beta_l^2-\beta_j^2) = 2(\pi^2/\mathcal{D}^2)(-1)^{l-j+1}\left(l-\frac{1}{2}\right)\times\left(j-\frac{1}{2}\right)(1-\delta_{jl})$, and therefore we get Eq. (29).

APPENDIX B: TECHNICAL PROOF

1. Expression [Eq. (22)] of the modal amplitudes

Given the form of Eq. (21) of the surface perturbation, the modal amplitudes have the form

$$\hat{a}_j(\omega,x,y) = \hat{A}_j(\omega,x)\exp\left(i\hat{B}_j(\omega,x)y^2 + i\hat{C}_j(\omega,x)y\right), \qquad \text{(B1)}$$

where $(\hat{A}_j,\hat{B}_j,\hat{C}_j)$ are given by

$$\begin{aligned}&\hat{A}_j(\omega,x) = \frac{e^{-3i\pi/4}}{2\sqrt{2\pi\beta_j(\omega)x}}\hat{f}_j(\omega), \quad \hat{B}_j(\omega,x) = \frac{\beta_j(\omega)}{2x},\\ &\hat{C}_j(\omega,x) = 0, \qquad \text{(B2)}\end{aligned}$$

for $x\in(0,L_0)$, $(\hat{A}_j,\hat{B}_j,\hat{C}_j)$ satisfy

$$\begin{cases} \partial_x \hat{B}_j = -\dfrac{2\hat{B}_j^2}{\beta_j} - \dfrac{q_{jj}}{2\beta_j \lambda_o L}\mu_2(x), \\ \partial_x \hat{C}_j = -\dfrac{2\hat{B}_j \hat{C}_j}{\beta_j} - \dfrac{q_{jj}}{2\beta_j \sqrt{\lambda_o L}}\mu_1(x), \\ \dfrac{\partial_x \hat{A}_j}{\hat{A}_j} = -\dfrac{2\hat{B}_j + i\hat{C}_j^2}{2\beta_j} - i\dfrac{q_{jj}}{2\beta_j}\mu_0(x) \end{cases} \tag{B3}$$

for $x \in (L_0, L_1)$, and $(\hat{A}_j, \hat{B}_j, \hat{C}_j)$ satisfy

$$\begin{cases} \hat{A}_j(\omega, x) = \dfrac{\hat{A}_j(\omega, L_1)}{\sqrt{1 + \dfrac{2B_j(\omega, L_1)}{\beta_j(\omega)}(x - L_1)}} \\ \quad \times \exp\left(-i\dfrac{\hat{C}_j(\omega, L_1)^2}{2\beta_j(\omega)} \dfrac{x - L_1}{1 + \dfrac{2\hat{B}_j(\omega, L_1)}{\beta_j(\omega)}(x - L_1)}\right), \\ \hat{B}_j(\omega, x) = \dfrac{\hat{B}_j(\omega, L_1)}{1 + \dfrac{2\hat{B}_j(\omega, L_1)}{\beta_j(\omega)}(x - L_1)}, \\ \hat{C}_j(\omega, x) = \dfrac{\hat{C}_j(\omega, L_1)}{1 + \dfrac{2\hat{B}_j(\omega, L_1)}{\beta_j(\omega)}(x - L_1)}. \end{cases} \tag{B4}$$

for $x \in (L_1, L)$. Note that $\hat{B}_j$ and $\hat{C}_j$ are real-valued. The important equation is the Ricatti equation satisfied by $\hat{B}_j$ in $x \in (L_0, L_1)$. The solution is of the form $\hat{B}_j = (\beta_j/2)(\partial_x \hat{D}_j / \hat{D}_j)$, where $\hat{D}_j$ satisfies the second-order differential equation

$$\partial_x^2 \hat{D}_j = -\frac{q_{jj}}{\beta_j^2 \lambda_o L}\mu_2(x)\hat{D}_j, \quad \hat{D}_j(L_0) = L_0, \quad \partial_x \hat{D}_j(L_0) = 1.$$

If, additionally, $L_1 - L_0$ is smaller than L, then we find $\hat{A}_j(L_1) = \frac{e^{-3i\pi/4}}{2\sqrt{2\pi\beta_j L_1}} \exp\left(-i\frac{q_{jj}}{2\beta_j}\nu_0\right)\hat{f}_j$, $\hat{B}_j(L_1) = \frac{\beta_j}{2L_1} - \frac{q_{jj}}{2\beta_j \lambda_o L}\nu_2$, and

$$\hat{A}_j(\omega, L) = \frac{\hat{A}_{j,o}(\omega, L)}{\sqrt{1 - \dfrac{q_{jj}\nu_2}{\beta_j(\omega)^2}\dfrac{L_1(L - L_1)}{\lambda_o L^2}}} \exp\left(-i\frac{q_{jj}}{2\beta_j(\omega)}\nu_0\right), \tag{B5}$$

where $\hat{A}_{j,o}(\omega, L)$ is defined by Eq. (23). This gives the desired result.

2. Properties of the source [Eq. (37)]

Here, we want to show that the source [Eq. (37)] produces a focal spot centered at the point $(x, y, z) = (x_0, 0, \mathcal{D})$. The unperturbed wavefield transmitted by the source $\hat{f}_j$ given by Eq. (37) is

$$\hat{p}_o(x, 0, z) = \frac{e^{-3i\pi/4}}{2\sqrt{2\pi x}} \sum_{j=1}^{M} \hat{f}_j \exp(i\beta_j x)\phi_j(z).$$

As $\partial_z \phi_j(\mathcal{D}) = \left(\sqrt{2}\pi / \mathcal{D}^{3/2}\right)\left(j - \frac{1}{2}\right)(-1)^j$ and $\hat{f}_j$ are given by Eq. (37), we have

$$\begin{aligned} &\partial_z \hat{p}_o(x_0 + x', 0, \mathcal{D}) \\ &= \frac{e^{-3i\pi/4}}{2\sqrt{2\pi(x_0 + x')}} \sum_{j=1}^{M} \hat{f}_j \exp(i\beta_j(x_0 + x'))\partial_z \phi_j(\mathcal{D}) \\ &= \frac{-i\sqrt{\pi}}{2\sqrt{x_0 + x'}\mathcal{D}^{3/2}} \sum_{j=1}^{M} \exp(i\beta_j x')\sqrt{\beta_j}. \end{aligned}$$

If $N \gg 1$ ($N = [k\mathcal{D}/\pi]$) and $\alpha = M/N = 1$, then

$$\partial_z \hat{p}_o(x_0 + x', 0, \mathcal{D}) = \frac{-i}{2\sqrt{\pi}} \frac{k^{3/2}}{\sqrt{\mathcal{D}x_0}} \psi_0(kx'),$$

$$\psi_0(X) = \int_0^1 e^{i\sqrt{1-s^2}X} \sqrt[4]{1 - s^2} ds,$$

which shows that the radius of the focal spot is on the order of the wavelength in the range direction x. If $\alpha = M/N \ll 1$, then

$$\partial_z \hat{p}_o(x_0 + x', 0, \mathcal{D}) \simeq \frac{-i}{2\sqrt{\pi}} \frac{k^{3/2}\alpha}{\sqrt{\mathcal{D}x_0}} e^{ikx'} \psi(\alpha^2 kx'),$$

with ψ defined by Eq. (D1). This shows that the radius is on the order of the wavelength divided by $\alpha^2 = (M/N)^2$ in the range direction x. Similarly, we get

$$\begin{aligned} \partial_z \hat{p}_o(x_0, 0, \mathcal{D} + z') &= \frac{e^{-3i\pi/4}}{2\sqrt{2\pi x_0}} \sum_{j=1}^{M} \hat{f}_j \exp(i\beta_j x_0)\partial_z \phi_j(\mathcal{D} + z') \\ &\simeq \frac{-i}{2\sqrt{\pi}} \frac{k^{3/2}\alpha}{\sqrt{\mathcal{D}x_0}} \mathrm{sinc}(\alpha k z'). \end{aligned}$$

This shows that the radius is on the order of the wavelength divided by α in the depth direction z.

3. Resolution analysis and proof of Eq. (39)

We substitute the second term in the right-hand side of Eq. (29), which is the perturbed modal amplitude A_j^{per}, and the expression of Eq. (37) of the source into Eq. (38),

$$\mathcal{I}(x_0) = \frac{\pi^{3/2}}{2\sqrt{2}\mathcal{D}^2} \sum_{j,l=1}^{M} \int_0^L \frac{\mu_0(x)}{\sqrt{\beta_j x + \beta_l (L - x)}} e^{i(\beta_l - \beta_j)(x - x_0)} dx.$$

When $M \ll N$, we can approximate β_j by k in the denominator, and we find

$$\mathcal{I}(x_0) = \frac{\pi^{3/2}}{2\sqrt{2}\mathcal{D}^2\sqrt{kL}} \int_0^L \mu_0(x) \left| \sum_{j=1}^{M} e^{i\beta_j(x - x_0)} \right|^2 dx.$$

We finally use Lemma D to get the desired result.

https://doi.org/10.1121/10.0010533

4. Special functions

In this subsection, we state and prove two technical lemmas used in the paper.

Lemma C. *If $1 \ll M \ll N$, then the kernel $a_{\mathcal{F}}$ defined by Eq. (35) satisfies*

$$a_{\mathcal{F}}(x,x') \simeq \frac{k^3\mathcal{D}^2\alpha^6}{72\pi^3 L}\psi_{\mathcal{F}}\big(\alpha^2 k|x-x'|\big), \tag{C1}$$

with $\alpha = M/N$ $(\alpha \ll 1)$, $\psi_{\mathcal{F}}(X) = |3\int_0^1 s^2 \exp(iXs^2/2)ds|^2$, *which is such that* $\psi_{\mathcal{F}}(0)=1$, $\psi_{\mathcal{F}}(X) \simeq 9/X^2$ *as* $X \to +\infty$, *and* $\int_{\mathbb{R}}\psi_{\mathcal{F}}(X)dX = 9\pi/2$.

Proof. Using $M \ll N$, we have $\beta_j \simeq k - \frac{\pi^2}{2k\mathcal{D}^2}(j-\frac{1}{2})^2$ for all $j \le M$, and therefore (with $N \simeq k\mathcal{D}/\pi$)

$$\begin{aligned} a_{\mathcal{F}}(x,x') &\simeq \sum_{j,l=1}^{M}\frac{\pi^3}{8k^3\mathcal{D}^4 L}\left(j-\frac{1}{2}\right)^2\left(l-\frac{1}{2}\right)^2 \\ &\quad\times \exp\left[i\frac{\pi^2(x'-x)}{2k\mathcal{D}^2}\left(\left(j-\frac{1}{2}\right)^2-\left(l-\frac{1}{2}\right)^2\right)\right] \\ &\simeq \frac{\pi^3 N^6\alpha^6}{72k^3\mathcal{D}^4 L}\left|\frac{3}{\alpha^3}\int_0^\alpha s^2\exp\left(i\frac{k(x'-x)}{2}s^2\right)ds\right|^2 \\ &\simeq \frac{k^3\mathcal{D}^2\alpha^6}{72\pi^3 L}\left|3\int_0^1 s^2\exp\left(i\frac{\alpha^2 k(x'-x)}{2}s^2\right)ds\right|^2, \end{aligned}$$

which gives the first desired result. The behavior of $\psi_{\mathcal{F}}(X)$ for large X follows from an integration by parts formula,

$$\begin{aligned} \psi_{\mathcal{F}}(X) &= \left|\frac{3\sqrt{2}}{X^{3/2}}\int_0^{X/2}\sqrt{u}\exp(iu)du\right|^2 \\ &= \frac{18}{X^3}\left|\frac{1}{i}\left[\sqrt{u}e^{iu}\right]_0^{X/2}+\frac{i}{2}\int_0^{X/2}\frac{e^{iu}}{\sqrt{u}}du\right|^2 \\ &= \frac{9}{X^2}(1+o(1)). \end{aligned}$$

Finally, $\int_{\mathbb{R}}dX\psi_{\mathcal{F}}(X) = 18\int_{\mathbb{R}}dX\int_0^{1/2}dS\int_0^{1/2}dS'\sqrt{SS'}\cos[X(S-S')] = 36\pi\int_0^{1/2}SdS = 9\pi/2$. □

Lemma D. *If $1 \ll M \ll N$, then*

$$\frac{1}{M}\sum_{j=1}^{M}e^{i\beta_j x} \simeq e^{ikx}\psi(\alpha^2 kx),$$

$$\psi(X) = \sqrt{2}\frac{C(X/\sqrt{2})-iS(X/\sqrt{2})}{X}, \tag{D1}$$

where $\alpha = M/N$ *and* C *and* S *are Fresnel integrals* $C(X) = \int_0^X\cos(s^2)ds$, $S(X) = \int_0^X\sin(s^2)ds$.

Proof. We can expand β_j because $M \ll N$, and we can replace the discrete sum by a continuous integral because $M \gg 1$, so we obtain

$$\frac{1}{M}\sum_{j=1}^{M}e^{i\beta_j x} \simeq \frac{1}{M}e^{ikx}\sum_{j=1}^{M}e^{-i(j-\frac{1}{2})^2\frac{\pi^2 x}{2\mathcal{D}^2 k}} \simeq e^{ikx}\int_0^1 e^{-is^2\frac{M^2\pi^2 x}{2\mathcal{D}^2 k}}ds,$$

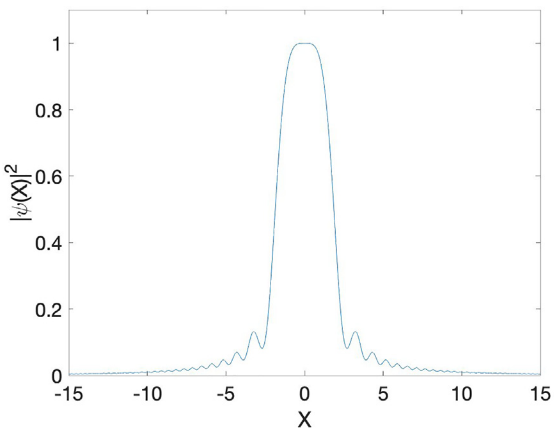

FIG. 7. (Color online) Function $|\psi(X)|^2$ with ψ defined by Eq. (B7).

which gives the desired result, as $(M^2\pi^2/\mathcal{D}^2k) \simeq \alpha^2 k$. □

The function $|\psi(X)|^2$ is plotted in Fig. 7. We have $\psi(0)=1$, and straightforward calculation shows that $\int_{\mathbb{R}}|\psi(X)|^2dX = \pi^{3/2}$.

[1] E. I. Thorsos, "The validity of the Kirchhoff approximation for rough surface scattering using a Gaussian roughness spectrum," J. Acoust. Soc. Am. **83**, 78–92 (1988).
[2] E. I. Thorsos and D. R. Jackson, "The validity of the perturbation approximation for rough surface scattering using a Gaussian roughness spectrum," J. Acoust. Soc. Am. **86**, 261–277 (1989).
[3] G. B. Deane, J. C. Preisig, C. T. Tindle, A. Lavery, and M. D. Stokes, "Deterministic forward scatter from surface gravity waves," J. Acoust. Soc. Am. **132**, 3673–3686 (2012).
[4] P. Roux and B. Nicolas, "Inverting for a deterministic surface gravity wave using the sensitivity-kernel approach," J. Acoust. Soc. Am. **135**, 1789–1799 (2014).
[5] C. T. Tindle and G. B. Deane, "Shallow water sound propagation with surface waves," J. Acoust. Soc. Am. **117**, 2783–2794 (2005).
[6] S. P. Walstead and G. B. Deane, "Surface wave profile reconstruction," J. Acoust. Soc. Am. **133**(5), 2597–2611 (2013).
[7] C. T. Tindle, G. B. Deane, and J. C. Preisig, "Reflection of underwater sound from surface waves," J. Acoust. Soc. Am. **125**, 66–72 (2009).
[8] J. C. Preisig and G. B. Deane, "Surface wave focusing and acoustic communications in the surf zone," J. Acoust. Soc. Am. **116**, 2067–2080 (2004).
[9] S. P. Walstead and G. B. Deane, "Determination of ocean surface wave shape from forward scattered sound," J. Acoust. Soc. Am. **140**(2), 787–797 (2016).
[10] J. Sarkar, C. Marandet, P. Roux, S. Walker, B. D. Cornuelle, and W. A. Kuperman, "Sensitivity kernel for surface scattering in a waveguide," J. Acoust. Soc. Am. **131**(1), 111–118 (2012).
[11] P. Roux, B. D. Cornuelle, W. A. Kuperman, and W. S. Hodgkiss, "The structure of raylike arrivals in a shallow-water waveguide," J. Acoust. Soc. Am. **124**(6), 3430–3439 (2008).
[12] P. Roux, W. A. Kuperman, B. D. Cornuelle, F. Aulanier, W. S. Hodgkiss, and H. C. Song, "Analyzing sound speed fluctuations in shallow water from group-velocity versus phase-velocity data representation," J. Acoust. Soc. Am. **133**, 1945-1952 (2013).
[13] T. van Baarsel, P. Roux, J. I. Mars, and B. Nicolas, "Surface perturbation inverted from angle variations of eigenbeams in an ultrasonic waveguide," J. Acoust. Soc. Am. **148**, 2841–2850 (2020).
[14] T. van Baarsel, P. Roux, J. I. Mars, J. Bonnel, M. Arrigoni, S. Kerampran, and B. Nicolas, "Dynamic imaging of a capillary-gravity wave in shallow water using amplitude variations of eigenbeams," J. Acoust. Soc. Am. **146**, 3353–3361 (2019).
[15] C. L. Pekeris, "Theory of propagation of explosive sound in shallow water," in *Propagation of Sound in the Ocean* (Geological Society of America, Boulder, CO, 1948).
[16] F. Aulanier, B. Nicolas, P. Roux, and J. I. Mars, "Time-angle sensitivity kernels for sound-speed perturbations in a shallow ocean," J. Acoust. Soc. Am. **134**(1), 88–96 (2013).

[17]J. Garnier, "Low-frequency source imaging in a waveguide," Inverse Probl. **36**, 115004 (2020).
[18]C. Tsogka, D. A. Mitsoudis, and S. Papadimitropoulos, "Partial-aperture array imaging in acoustic waveguides," Inverse Probl. **32**, 125011 (2016).
[19]L. Borcea and J. Garnier, "Paraxial coupling of propagating modes in three-dimensional waveguides with random boundaries," Multiscale Model. Simul. **12**, 832–878 (2014).
[20]L. B. Dozier and F. D. Tappert, "Statistics of normal mode amplitudes in a random ocean," J. Acoust. Soc. Am. **63**, 353-365 (1978).
[21]J.-P. Fouque, J. Garnier, G. Papanicolaou, and K. Sølna, *Wave Propagation and Time Reversal in Randomly Layered Media* (Springer, New York, 2007).
[22]J. Garnier and G. Papanicolaou, "Pulse propagation and time reversal in random waveguides," SIAM J. Appl. Math. **67**, 1718-1739 (2007).
[23]C. Gomez, "Wave propagation in shallow-water acoustic random waveguides," Commun. Math. Sci. **9**, 81-125 (2011).
[24]C. Gomez, "Wave propagation in shallow-water acoustic waveguides with rough boundaries," Commun. Math. Sci. **13**, 2005-2052 (2015).
[25]W. Kohler and G. Papanicolaou, "Wave propagation in randomly inhomogeneous ocean," in *Wave Propagation and Underwater Acoustics*, Lecture Notes in Physics Vol. 70, edited by J. B. Keller and J. S. Papadakis (Springer Verlag, Berlin, 1977).
[26]R. Alonso, L. Borcea, and J. Garnier, "Wave propagation in waveguides with random boundaries," Commun. Math. Sci. **11**, 233–267 (2013).